

## QUANTUM MECHANICS

## Schrödinger cat states of a 16-microgram mechanical oscillator

Marius Bild<sup>1,2†</sup>, Matteo Fadel<sup>1,2,\*</sup>, Yu Yang<sup>1,2†</sup>, Uwe von Lüpke<sup>1,2</sup>, Phillip Martin<sup>1,2</sup>, Alessandro Bruno<sup>1,2</sup>, Yiwen Chu<sup>1,2\*</sup>

According to quantum mechanics, a physical system can be in any linear superposition of its possible states. Although the validity of this principle is routinely validated for microscopic systems, it is still unclear why we do not observe macroscopic objects to be in superpositions of states that can be distinguished by some classical property. Here we demonstrate the preparation of a mechanical resonator in Schrödinger cat states of motion, where the  $\sim 10^{17}$  constituent atoms are in a superposition of two opposite-phase oscillations. We control the size and phase of the superpositions and investigate their decoherence dynamics. Our results offer the possibility of exploring the boundary between the quantum and classical worlds and may find applications in continuous-variable quantum information processing and metrology with mechanical resonators.

Quantum mechanics is one of the most successful scientific theories ever formulated. However, from the early days of quantum mechanics until now, it has been unclear why quantum phenomena, such as state superpositions, are never observed in the macroscopic world. In his 1935 work (1), Erwin Schrödinger imagined a device able to poison a cat as a consequence of a radioactive decay, concluding that the superposition of an atom being “decayed” and “not decayed” could be mapped onto a superposition of the cat being simultaneously “dead” and “alive.” There are two aspects of this hypothetical scenario that make it seem absurd and counterintuitive: First, a cat is a macroscopic, everyday object; and second, “dead” and “alive” are states that are mutually exclusive within our classical experience.

Many explanations have been proposed as to why we may never encounter a cat in such an unfortunate situation. Macroscopic objects may simply be too complex and subject to too many sources of decoherence to sustain a superposition of classically distinct states. Other theories introduce additional effects beyond standard quantum mechanics, such as wave function collapse due to intrinsic stochastic noise or gravitational decoherence (2). These effects are typically expected to scale with the mass of the system and the distinctness of the states that are superposed. Therefore, observing state superpositions in massive objects is of key importance for exploring the validity range of quantum mechanics as we know it. Beyond its fundamental interest, preparing and detecting Schrödinger’s cat states is essential

for applications in quantum technologies. Main examples include Heisenberg-limited parameter estimation protocols (3, 4) and error-protected quantum information processing (5, 6).

There have been many experimental demonstrations of Schrödinger cat states (which we will call “cat states” from here on). These include superpositions of internal and motional degrees of freedom in trapped ions (7, 8), phase-space superpositions of electromagnetic waves in both the optical (9, 10) and microwave domains (11–13), Greenberger–Horne–Zeilinger states (14, 15), current superpositions in superconducting quantum interference devices (16), and spatial superpositions of atomic clouds (17) and large molecules (18). We experimentally demonstrate the preparation of cat states in the motional degree of freedom of a solid-state mechanical resonator. Given the variety of definitions found in previous works, we define a cat state of a harmonic oscillator as

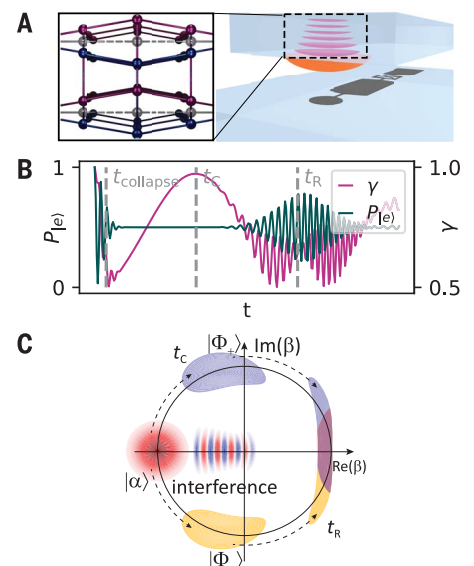
a coherent superposition of two or more states with well-separated phase-space distributions.

## Experimental setup

Our device, which we call a  $\hbar$ BAR, as in previous works (19), consists of a high-overtone bulk acoustic-wave resonator (HBAR) coupled to a superconducting transmon qubit. The transmon qubit allows us to create, control, and read out phonon states in the HBAR. Qubit and HBAR are fabricated on separate sapphire chips, which are subsequently flip chip bonded into the final device (Fig. 1A). A dome of piezoelectric aluminum nitride on the HBAR chip coherently couples the electric field of the qubit with the strain field of the resonator modes. The device is placed inside a three-dimensional Al cavity, which allows us to control the qubit with the standard circuit quantum electrodynamics toolbox (20). The acoustic free spectral range is  $\sim 12$  MHz, and frequency tuning the qubit via a microwave drive-induced Stark shift allows us to address several longitudinal phononic modes. The acoustic lattice oscillations are localized within a Gaussian mode with waist  $w_0 = 27 \mu\text{m}$  and length  $L = 435 \mu\text{m}$ , giving a mode volume of  $\pi w_0^2 L \approx 0.001 \text{ mm}^3$  [see supplementary text (21) section B for details]. More details about this circuit quantum acoustodynamics (cQAD) system (19, 22) and the device (23) can be found in previous works.

In the classical picture, one can imagine a coherent state  $|\alpha\rangle$  in the phonon mode as a coherent displacement of the atomic lattice with an amplitude proportional to  $\alpha$ . In the quantum picture, an example of a cat state is a quantum superposition of two coherent states with opposite displacement amplitudes, leading to the physical interpretation of such a state as the superposition of two oscillations

**Fig. 1. Illustration of the  $\hbar$ BAR device and system evolution.** (A) Schematics of the  $\hbar$ BAR device. The HBAR chip (top) has a layer of piezoelectric aluminum nitride (orange) and supports standing acoustic waves (pink). The transmon qubit on the lower chip has a circular antenna to couple with the HBAR. The inset shows the superposition of two opposite-phase oscillations of atoms in the crystal lattice. (B) Simulated evolution without decoherence of the qubit  $|e\rangle$  state population  $P_{|e\rangle}$  and purity  $\gamma$  under the JC interaction when the qubit is initialized in  $|{-}Z\rangle$  and the phonon in a coherent state. (C) Illustration of the evolution of an initial phonon coherent state (red circle on the left) in phase space. The blue (yellow) crescent shapes indicate the state  $|\Phi_{+}\rangle$  ( $|\Phi_{-}\rangle$ ), which is the phonon state when the qubit is initialized in  $|{+}X\rangle$  ( $|{-}X\rangle$ ). Interference fringes appear around time  $t_c$  when the qubit is prepared in a superposition of  $|{+}X\rangle$  and  $|{-}X\rangle$ . Around the revival time  $t_R$ , the two phonon states again overlap (purple).



<sup>1</sup>Department of Physics, ETH Zürich, 8093 Zürich, Switzerland. <sup>2</sup>Quantum Center, ETH Zürich, 8093 Zürich, Switzerland.

\*Corresponding author. Email: fadelm@phys.ethz.ch (M.F.); yiwen.chu@phys.ethz.ch (Y.C.)

†These authors contributed equally to this work.

of the atomic lattice with the same frequency  $\omega_p$  and relative phase  $\pi$ . Considering a snapshot in time where both oscillations are at their displacement maximum, Schrödinger's cat being in a superposition of dead and alive is analogous to a superposition of atoms in the HBAR being in two distinct positions in space, as illustrated in the inset of Fig. 1A. Here, we define the positions as distinct when their separation is larger than the fluctuations due to quantum, thermal, or other sources of noise.

### Generating cat states

To realize a cat state in our system, we use the Jaynes-Cummings (JC) interaction with the qubit and phonon on resonance (11, 24). The interaction Hamiltonian is

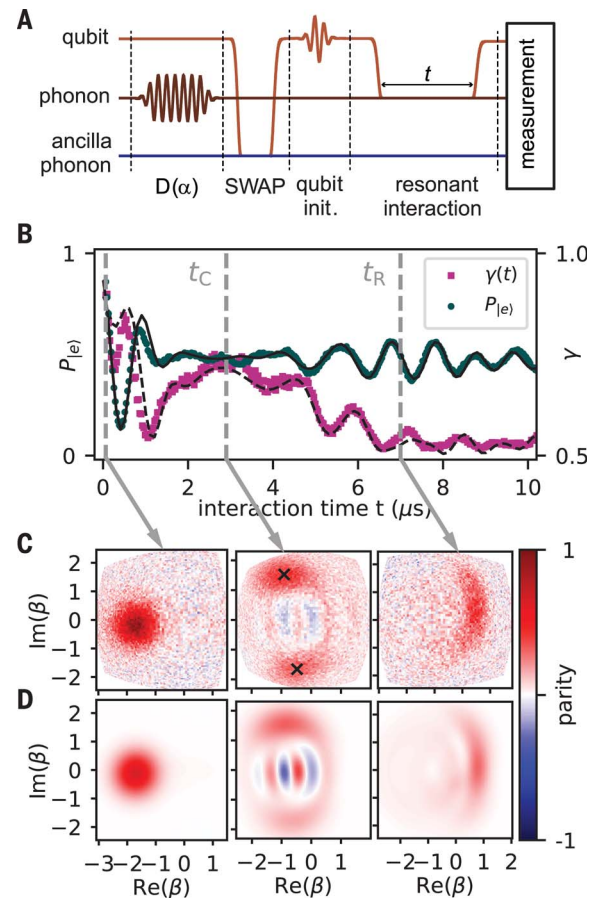
$$H/\hbar = g_0(\sigma^+ a + \sigma^- a^\dagger) \quad (1)$$

where  $g_0$  is the coupling strength between qubit and phonon mode,  $\sigma^+$  is the raising operator for the qubit, and  $a^\dagger$  is the raising operator for the phonon mode. This results in Rabi oscillations between the states  $|e, n-1\rangle$  and  $|g, n\rangle$  at a rate  $g_0\sqrt{n}$ , where  $|g\rangle$  ( $|e\rangle$ ) is the qubit ground (excited) state and  $|n\rangle$  is the Fock state of  $n$  phonons. As a consequence of this  $\sqrt{n}$  scaling, if the phonon mode is prepared in a coherent state with large enough amplitude and the qubit is prepared in  $|g\rangle$  or  $|e\rangle$ , their coherent interaction rapidly dephases. Hence, the oscillations of the qubit population “collapse” (Fig. 1B) with a decaying amplitude proportional to  $(25, 26) \exp(-(t/t_{\text{collapse}})^2)$ , where  $t_{\text{collapse}} = \sqrt{2}/g_0$  is the collapse time in the limit of  $\alpha \gg 1$ . At this time, the qubit and phonon states are entangled. This can be seen in Fig. 1B as a minimum in the qubit state purity  $\gamma(t) = \text{Tr}(\rho_q(t)^2)$  around  $t_{\text{collapse}}$ , where  $\rho_q(t)$  is the reduced density matrix of the qubit. Notably, owing to the quantized phonon energy and the consequent discrete oscillation frequency spectrum, the oscillations revive in finite time (24). For  $\alpha \gg 1$ , this revival occurs at  $t_R = 2\pi\alpha/g_0$  (27). Between the collapse and revival, at time  $t_R/2$ , the qubit and phonon disentangle from each other. The state being separable at  $t_R/2$  coincides with the occurrence of a superposition of two distinct states in phase space, realizing a cat state in the phonon mode (11, 21, 24, 28).

A more intuitive explanation for the origin of the cat state comes from the time evolution of the reduced phonon state in phase space. As illustrated in Fig. 1C and shown in supplementary text section A, if the qubit is initialized in the state  $|\pm Z\rangle \equiv (|e\rangle \pm |g\rangle)/\sqrt{2}$  and in the limit of large  $\alpha$ , the evolution leads to a rotation in phase space with an angular velocity  $\mp|g_0/2\alpha|$  and a distortion of the coherent states. We call the resulting states  $|\Phi_\pm(t)\rangle$ , whose full expressions are given in the supplement-

### Fig. 2. Collapse and revival dynamics.

(A) Experimental sequence for observing collapse and revivals dynamics and for preparing cat states (details in the main text). (B) Measured qubit population and state purity. The solid and dashed black lines are the simulation results of the qubit population and purity, respectively. Three time points of particular interest are highlighted (dashed lines): initial state time, cat state time ( $t_C$ ), and revival state time ( $t_R$ ). (C) Measured Wigner function of the phonon state at the three time points. Axes are the real and imaginary parts of the complex displacement amplitude  $\beta$  used during Wigner tomography (23). The black crosses indicate the positions of the two coherent states composing the fitted CSS state Eq. 2) (D) Corresponding simulated Wigner functions.



tary text (eq. S15). If the qubit is initialized in the state  $|\pm Z\rangle \equiv (|+X\rangle \pm |-X\rangle)/\sqrt{2}$ , the phonon state will evolve into  $|\Phi_+(t)\rangle \pm |\Phi_-(t)\rangle$  as shown in Fig. 1C. At time  $t_R/2$ , the two state components  $|\Phi_\pm\rangle$  have covered a rotation angle of  $\mp\pi/2$  around a circle of radius  $\alpha$ , maximizing their separation in phase space and forming a cat state (24). Finally, at the revival time  $t_R$ , the two phonon state components  $|\Phi_\pm\rangle$  have both rotated by a phase of  $\pi$  and approximately recombine in phase space.

### Experimental results

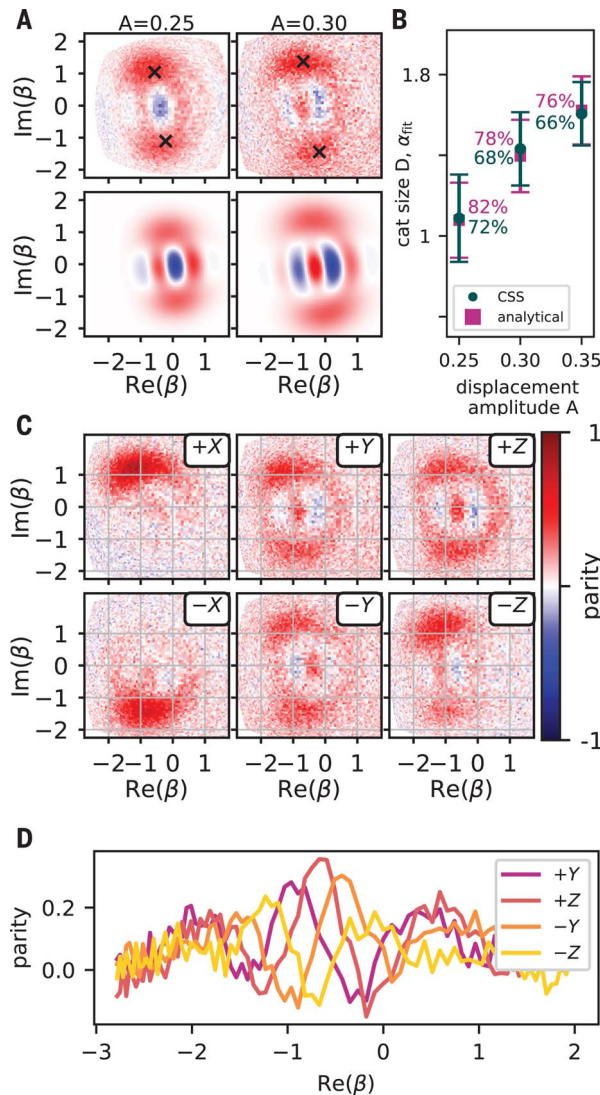
We experimentally confirm both the predicted collapse and revival of Rabi oscillations and the creation of mechanical cat states in the phonon mode. The basic sequence used in the experimental demonstration of the JC dynamics described above can be seen in Fig. 2A. We displace the phonon mode with a resonant drive of amplitude  $A$  to a coherent state with amplitude  $\alpha$ . To mitigate any effect of the drive on the qubit state, we then cool the qubit with an ancillary phonon mode (22, 23). The qubit is subsequently prepared in its initial state by applying a drive pulse with variable phase and amplitude. To induce the resonant interaction, we tune the qubit to the phonon mode frequency for a variable interaction time  $t$ . Depending on which of the subsystems we want to char-

acterize, we choose a measurement sequence that implements the appropriate measurement operator. First, we simply measure the qubit excited state population. The resulting data are shown in Fig. 2B for  $A = 0.35$ . Here the value for  $A$  is a scaling factor for the amplitude of a microwave drive, which we calibrate to find a corresponding initial coherent state size of  $\alpha = 1.75$  (supplementary text section E). As expected, we observe oscillations that collapse after a time  $t_{\text{collapse}} \approx 0.9 \mu\text{s}$  and revive at  $t_R \approx 6.7 \mu\text{s}$ . This revival indicates the coherent exchange of energy quanta between the qubit and phonon mode during the resonant interaction. By performing full qubit tomography after the resonant interaction, we can also reconstruct the reduced density matrix of the qubit subsystem  $\rho_q$  and calculate the purity of the qubit state  $\gamma(t)$ . We confirm a local minimum of  $\gamma(t)$  around the predicted collapse time  $t_{\text{collapse}}$ , followed by a local maximum around  $t_R/2$  (Fig. 2B).

We now focus on the time evolution of the phonon subsystem by performing full Wigner tomography of the phonon state after the resonant interaction times  $t = 0, 2.9$  and  $7.0 \mu\text{s}$ . To this end, we use the parity measurement technique established in a previous work (23). To compensate for the effect of qubit dephasing during the parity measurement, we normalize



**Fig. 3. Cat state amplitude and phase control.** (A) Cat states prepared with different displacement pulse amplitudes  $A$ . Top row: Measured Wigner functions; bottom row: analytical state  $\rho(t_c)$  that best fits the data. The fitted CSS states, with coherent state positions indicated by black crosses, have  $D = 1.09$  (1.43) for  $A = 0.25$  (0.30). (B) Cat state sizes as a function of the displacement amplitude  $A$ , obtained from fitting the data in (A) to analytical states  $\rho(t_c)$  and CSS states  $|C\rangle$ . Numbers are the fidelity with respect to the fitted state. Error bars show cat state sizes resulting in 1 % deviation in the fidelity (supplementary text section G). (C) Cat states resulting from the initial qubit states indicated by the respective labels. (D) Cross-cuts of interference fringes from (C) for four initial qubit states, obtained by averaging the data between  $-0.11 < \text{Im}(\beta) < 0.16$ .



all measured parity values to that of the Fock  $|0\rangle$  phonon state (supplementary text section D). The measured Wigner functions are shown in Fig. 2C, where axes in phase space are normalized by measuring the distribution of populations in the phonon Fock states for coherent states created with different drive amplitudes (22) (supplementary text section E).

From the measured data, we confirm the evolution of the initial coherent state (Fig. 2C, left) into a cat state at  $t_c = 2.9 \mu\text{s}$  (Fig. 2C, center), showing two state components clearly distinct in phase space and interference fringes located between them. We choose this value of  $t_c$  because it corresponds to the measured maximum in the qubit state purity. It deviates somewhat from the value predicted by using the large  $\alpha$  limit, which is  $t_R/2 \approx 3.3 \mu\text{s}$ . For the evolution time  $t = 7.0 \mu\text{s}$ , the predicted refocusing into a crescent-shaped overlap between the counter-rotating state components can be observed (Fig. 2C, right).

To benchmark the cat state and obtain an estimate of its size, we implement a maximum-likelihood reconstruction (29) of the phonon state  $\rho_p$  from the measured state with  $A = 0.35$  and  $t_c = 2.9 \mu\text{s}$ . We then fit the reconstructed state to an analytical expression of the expected phonon state  $\rho(t_c)$  in the absence of decoherence and after tracing out the qubit (supplementary text section A). Fixing the interaction time to  $t_c$  from the experiment, the fit maximizes the fidelity between  $\rho_p$  and  $\rho(t_c)$  by varying the initial coherent state size  $\alpha_{\text{fit}}$  of  $\rho(t_c)$ . The result yields a fidelity of  $\mathcal{F} \approx 76\%$  to an analytical state with initial coherent state size  $\alpha_{\text{fit}} = 1.62$ , which is smaller than the initial displacement  $\alpha = 1.75$  because the expression for  $\rho(t_c)$  does not include phonon losses. We attribute the infidelity to a combination of decoherence and measurement imperfections that lead to additional artifacts in the Wigner function (23). To further confirm that the phonon state behaves as ex-

pected, Fig. 2D shows the results of a master equation simulation of the full experimental protocol with independently measured system parameters, showing good agreement with the measurements in Fig. 2C.

The state we obtained resembles the two-component coherent state superpositions (CSS)

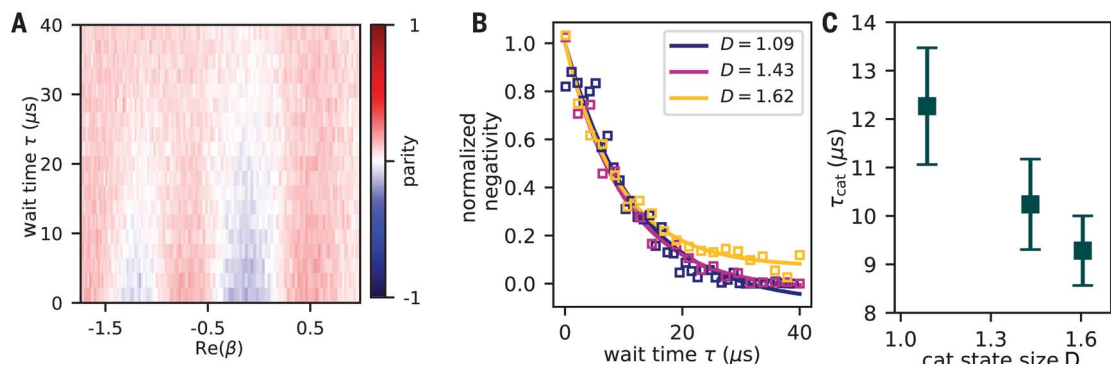
$$|C\rangle = \mathcal{N}(|\alpha_1\rangle + e^{i\vartheta}|\alpha_2\rangle) \quad (2)$$

a type of cat state that is often invoked in quantum information (5, 6) and parameter estimation protocols (3, 4). Here  $|\alpha_{1,2}\rangle$  are two coherent states and  $\mathcal{N}$  is the appropriate normalization constant. We can fit our reconstructed state to Eq. 2 by optimizing  $\alpha_1$ ,  $\alpha_2$ , and  $\vartheta$  for maximum fidelity  $\mathcal{F}(\rho_p, |C\rangle\langle C|)$ . Because our state is not centered around the origin in phase space, we use half the phase space distance between the coherent state components  $D = |\alpha_1 - \alpha_2|/2$  as a measure of the cat state size. This choice is motivated by considering a coherent state superposition centered around the origin in phase space, such that  $\alpha_1 = -\alpha_2$ . Then  $D = |\alpha_{1,2}| = \sqrt{\bar{n}}$ , where  $\bar{n}$  is the average phonon population of the state created. For the state in Fig. 2C, we obtain a state size  $D = 1.61$ , corresponding to  $\bar{n} = D^2 = 2.60$ , with a fidelity of  $\mathcal{F} \approx 66\%$ . The smaller state size  $D$  compared to the initial coherent displacement is a combination of decoherence and the choice of interaction time  $t_c < t_R/2$ , resulting in the two counter-rotating state components not reaching their maximum separation in phase space. The fidelity is lower compared to the fitted analytical state  $\rho(t_c)$ , because  $\rho(t_c)$  itself has a finite infidelity to the CSS state  $|C\rangle$ .

We can now translate the parameters of the measured cat state into physical properties of the phonon mode, such as the spatial separation between atoms. A state size of  $D = 1.61$  corresponds to a maximal delocalization of  $7.0 \cdot x_{\text{ZPF}}$ , where  $x_{\text{ZPF}}$  is the zero point motion of an equivalent one-dimensional (1D) quantum harmonic oscillator (supplementary text section B). Because we are not considering a center-of-mass mode, there is some freedom in choosing  $x_{\text{ZPF}}$ , which is then associated with an effective oscillating mass of the mode. If we choose the root-mean-square (RMS) value of the atomic displacements, we find an effective mass of  $M_{\text{eff}}^{\text{RMS}} = 16.2 \mu\text{g}$ , corresponding to  $\sim 10^{17}$  atoms, delocalized over a distance of  $2.1 \times 10^{-18} \text{ m}$  (supplementary text section B).

In applications such as bosonic encodings of a qubit state, full control over the phase and amplitude of the created cat state is required (5, 6, 30). In the following, we demonstrate this level of control in our experiment. By varying the amplitude  $A$  of the phonon displacement drive, we can control the amplitude of the initial coherent state and the size of the resulting cat state. For displacement amplitudes  $A = 0.25$  and  $0.30$ , we create cat states with  $D = 1.09$

**Fig. 4. Decoherence of cat states.** (A) Measured 1D cuts through the interference fringes of the  $D = 1.43$  cat state for a range of wait times between state creation and measurement. (B) Extracted negativities (squares) from each cut versus wait times for three cat state sizes, together with fitted exponential decays (solid lines). Both data and fitted curves are normalized to the fitted value at  $\tau = 0$ . (C) Characteristic decay times  $\tau_{\text{cat}}$  extracted from the fits in (B) for all three cat state sizes. Error bars are uncertainties extracted from the fit.



and 1.43, respectively (Fig. 3A). The fidelities of reconstructions of the measured states to both a CSS state and  $\rho(t_C)$  are given in Fig. 3B. The best fit  $\rho(t_C)$  is plotted in the lower row of Fig. 3A, showing good qualitative agreement with the data. As before, the finite fidelities and lower-contrast fringes of the measured states as compared to the best-fit  $\rho(t_C)$  arise mainly from decoherence of the state during measurement.

In the two-component cat state encoding of a qubit, the six cardinal points of the Bloch sphere are given by two coherent states  $|\alpha_1\rangle$  and  $|\alpha_2\rangle$ , along with their four superpositions with  $\pi/2$  difference in the phase  $\vartheta$  (Eq. 2). We can prepare similar states by initializing the transmon qubit state in all six cardinal points  $|\pm X\rangle, |\pm Y\rangle, |\pm Z\rangle$  of its Bloch sphere before performing the cat state generation protocol. The preparation of  $|\pm X\rangle$  and  $|\pm Y\rangle$  is calibrated using collapse and revival measurements as a function of the qubit drive phase (supplementary text section A). The results for  $A = 0.35$  and  $t_C = 2.10 \mu\text{s}$  are shown in Fig. 3C. We observe a distorted coherent state located on the upper (lower) half of phase space for the qubit initially in  $|\pm X\rangle$ . This separation in phase space is expected from the opposite rotation directions between the phonon states when the qubit is prepared in  $|\pm X\rangle$  (Fig. 1C). The  $|\pm Y\rangle, |\pm Z\rangle$  states then give rise to four cat states that differ in phase by  $\pi/2$ , as can be observed in the phases of the interference fringes in Fig. 3D. The initial energy of the qubit, and thus of the total system, is not the same for all six scenarios, resulting in slightly different sizes for the cat states. In the limit of large cat state size, this difference becomes negligible, and the phonon subspace maps onto that of the cat state encoding.

Superposition states are nonclassical states that are notoriously prone to decoherence. We now investigate the quantum-to-classical transition of different-sized cat states by letting them evolve freely for a varying wait time  $\tau$  before performing Wigner tomography. During this evolution, the qubit is far detuned from the phonon mode. In particular, we fo-

cus on a slice through the Wigner function's interference fringes at  $\text{Im}(\beta) = 0$ , which highlights the nonclassical features of the superposition. Figure 4A shows the time evolution of this slice for the  $D = 1.43$  cat state. We observe that the negative features disappear on a time scale much faster than  $T_1^{\text{ph}} \approx 84 \mu\text{s}$ , the energy relaxation time of the phonon mode.

As a measure for the nonclassicality of the state, we extract the time-dependent negativity (31), defined as  $\delta(t) \equiv \int (|W(\beta, t)| - W(\beta, t)) d\beta$ . Here,  $W(\beta, t)$  is the measured Wigner function of the cat state at time  $t$ , and the integration is over the 1D slice in phase space parameterized by the complex displacement amplitude  $\beta$ . Figure 4B shows the resulting  $\delta(t)$  for the three different cat state sizes of Fig. 3B. We fit each dataset to an exponential decay plus a constant offset. The offset in the measured Wigner values arises from the fact that our Wigner tomography is not performed in the ideal dispersive limit (23). The extracted decay time scales  $\tau_{\text{cat}}$  are plotted in Fig. 4C. We show in section H of the supplementary text that, in the limit of large  $|\alpha|$ ,  $\delta(\tau)$  decays exponentially with a time constant  $\tau_{\text{cat}} = T_1^{\text{ph}} / (2|\alpha|^2)$ . However, for small  $|\alpha|$ ,  $\tau_{\text{cat}}$  deviates from this expression and is in fact dependent on properties of the exact state, such as the phase of the superposition. The data in Fig. 4C show the expected qualitative behavior of faster-decaying negativity for larger-sized cat states, and we present a more detailed quantitative analysis in the supplementary text (21).

### Concluding remarks

Our results show the generation of cat states in a microgram-mass solid-state mechanical mode using the tools of cQAD and pave the way toward using such systems for tests of wave function collapse models (32). These tests would benefit from larger-sized cat states, resonators with higher masses (33), and longer phonon lifetimes. To facilitate comparison with other mechanical resonators and theoretical models that often consider center-of-mass motion, we note that the HBAR mode is a standing wave in which a half-wavelength section approxi-

mates a center-of-mass mode where all atoms oscillate in the same direction. Such a section has a mass on the order of 30 ng, obtained by dividing the total effective mass of  $16 \mu\text{g}$  by the longitudinal mode number of  $\sim 500$ .

The maximum size of the cat state that we can prepare is currently limited by our device parameters, including both the qubit and phonon decoherence rates. The latter is especially important given that, in general, the decoherence rate of the cat state is proportional to the square of the cat state size  $D$ . Furthermore, additional improvements to the properties of qubit and phonon resonator would enable alternative cat state generation protocols that can in principle lead to states with a higher fidelity to, for example, a CSS state (12, 13). We point out, however, that although CSS states represent a useful benchmark (because they have been extensively studied for applications such as quantum information and quantum metrology), many of their salient features are present already in the states that we have demonstrated. These include the phase-space separation of state components, which is important for error protection of encoded qubits (30, 34, 35), and the presence of interference fringes with high Fisher information, which is useful for quantum-enhanced sensing (4, 36, 37).

### REFERENCES AND NOTES

1. E. Schrödinger, *Naturwissenschaften* **23**, 807–812 (1935).
2. A. Bassi, K. Lochan, S. Satin, T. P. Singh, H. Ulbricht, *Rev. Mod. Phys.* **85**, 471–527 (2013).
3. L. Pezzè, A. Smerzi, *Atom Interferometry, Proceedings of the International School of Physics "Enrico Fermi," Varenna*, G. M. Tino, M. A. Kasevich, eds. (IOS Press, Amsterdam, 2014).
4. W. J. Munro, K. Nemoto, G. J. Milburn, S. L. Braunstein, *Phys. Rev. A* **66**, 023819 (2002).
5. P. T. Cochrane, G. J. Milburn, W. J. Munro, *Phys. Rev. A* **59**, 2631–2634 (1999).
6. M. Mirrahimi et al., *New J. Phys.* **16**, 045014 (2014).
7. C. Monroe, D. M. Meekhof, B. E. King, D. J. Wineland, *Science* **272**, 1131–1136 (1996).
8. H.-Y. Lo et al., *Nature* **521**, 336–339 (2015).
9. A. Ourjoumtsev, H. Jeong, R. Tualle-Broui, P. Grangier, *Nature* **448**, 784–786 (2007).
10. K. Huang et al., *Phys. Rev. Lett.* **115**, 023602 (2015).
11. A. Auffèves et al., *Phys. Rev. Lett.* **91**, 230405 (2003).
12. S. Deléglise et al., *Nature* **455**, 510–514 (2008).
13. B. Vlastakis et al., *Science* **342**, 607–610 (2013).
14. D. Leibfried et al., *Nature* **438**, 639–642 (2005).
15. W.-B. Gao et al., *Nat. Phys.* **6**, 331–335 (2010).

16. J. R. Friedman, V. Patel, W. Chen, S. K. Tolpygo, J. E. Lukens, *Nature* **406**, 43–46 (2000).
17. T. Kovachy *et al.*, *Nature* **528**, 530–533 (2015).
18. Y. Y. Fein *et al.*, *Nat. Phys.* **15**, 1242–1245 (2019).
19. Y. Chu *et al.*, *Science* **358**, 199–202 (2017).
20. A. Blais, A. L. Grimsmo, S. M. Girvin, A. Wallraff, *Rev. Mod. Phys.* **93**, 025005 (2021).
21. See supplementary materials.
22. Y. Chu *et al.*, *Nature* **563**, 666–670 (2018).
23. U. von Lüpke *et al.*, *Nat. Phys.* **18**, 794–799 (2022).
24. V. Bužek, H. Moya-Cessa, P. L. Knight, S. J. D. Phoenix, *Phys. Rev. A* **45**, 8190–8203 (1992).
25. F. W. Cummings, *Phys. Rev.* **140**, A1051–A1056 (1965).
26. G. Rempe, H. Walther, N. Klein, *Phys. Rev. Lett.* **58**, 353–356 (1987).
27. J. H. Eberly, N. B. Narozhny, J. J. Sanchez-Mondragon, *Phys. Rev. Lett.* **44**, 1323–1326 (1980).
28. J. Gea-Banacloche, *Phys. Rev. Lett.* **65**, 3385–3388 (1990).
29. K. S. Chou *et al.*, *Nature* **561**, 368–373 (2018).
30. A. Grimm *et al.*, *Nature* **584**, 205–209 (2020).
31. A. Kenfack, K. Zyczkowski, *J. Opt. B Quantum Semiclassical Opt.* **6**, 396–404 (2004).
32. B. Schirnski *et al.*, *Phys. Rev. Lett.* **130**, 133604 (2023).
33. C. Whittle *et al.*, *Science* **372**, 1333–1336 (2021).
34. N. Ofek *et al.*, *Nature* **536**, 441–445 (2016).
35. C. Flühmann *et al.*, *Nature* **566**, 513–517 (2019).
36. J. Joo, W. J. Munro, T. P. Spiller, *Phys. Rev. Lett.* **107**, 083601 (2011).
37. A. Facon *et al.*, *Nature* **535**, 262–265 (2016).
38. M. Bild *et al.*, Schrödinger cat states of a 16-microgram mechanical oscillator, Zenodo (2023); <https://doi.org/10.5281/zenodo.7701912>.

#### ACKNOWLEDGMENTS

We thank O. Romero-Isart, A. Grimm, and I. C. Rodrigues for useful discussions, and A. Brooks for help with figure making. Fabrication of devices was performed at the FIRST cleanroom of ETH Zürich and the BRNC cleanroom of IBM Zürich. **Funding:** M.B. was supported by the QuantERA II Program that has received funding from the European Union's Horizon 2020 research and innovation program under grant agreement no 101017733, and with the Swiss National Science Foundation. M.F. was supported by The Branco Weiss Fellowship–Society in Science, administered by the ETH Zürich. P.M. was supported by the ThinkSwiss fellowship. **Author**

**contributions:** U.v.L. fabricated the device. M.B., M.F., Y.Y., and U.v.L. performed the experiments and analyzed the data. All authors performed theoretical calculations and simulations. Y.C. conceived of the project and supervised the work. M.B., M.F., Y.Y., U.v.L., and Y.C. wrote the manuscript. **Competing interests:** The authors declare no competing interests. **Data and materials availability:** All data and software are available in the manuscript or the supplementary material or are deposited at Zenodo (38). **License information:** Copyright © 2023 the authors, some rights reserved; exclusive licensee American Association for the Advancement of Science. No claim to original US government works. <https://www.sciencemag.org/about/science-licenses-journal-article-reuse>

#### SUPPLEMENTARY MATERIALS

[science.org/doi/10.1126/science.adf7553](https://science.org/doi/10.1126/science.adf7553)  
 Supplementary Text  
 Figs. S1 to S8  
 Tables S1 and S2  
 References (39–46)

Submitted 10 November 2022; accepted 20 March 2023  
[10.1126/science.adf7553](https://doi.org/10.1126/science.adf7553)